

We are IntechOpen, the world's leading publisher of Open Access books Built by scientists, for scientists

6,900

Open access books available

186,000

International authors and editors

200M

Downloads

Our authors are among the

154

Countries delivered to

TOP 1%

most cited scientists

12.2%

Contributors from top 500 universities



WEB OF SCIENCE™

Selection of our books indexed in the Book Citation Index
in Web of Science™ Core Collection (BKCI)

Interested in publishing with us?
Contact book.department@intechopen.com

Numbers displayed above are based on latest data collected.
For more information visit www.intechopen.com



FEA in Micro-Electro-Mechanical Systems (MEMS) Applications: A Micromachined Spatial Light Modulator (μ SLM)

Hao Ren and Jun Yao

Additional information is available at the end of the chapter

<http://dx.doi.org/10.5772/48532>

1. Introduction

Since the Nobel Prize winner, Richard Feynman gave the presentation “there is plenty of room at the bottom” [1], a variety of micromachined sensors, actuators, and systems have emerged and made encouraging progress in the past 50 years, based on technological innovations and increased market demand [2]. To date, Micro-Electro-Mechanical Systems (MEMS) have been developed into an interdisciplinary subject which involves electrical, mechanical, thermal, optical, and biological knowledge. Due to its significant potential, which has partially been demonstrated by the success of inertial MEMS devices (accelerometers, gyroscopes, *etc* [3, 4]) radio frequency (RF) MEMS devices (switches, filters, resonators, *etc* [5-7]) and optical MEMS devices (Digital Light Processing, DLP [8, 9]), the research in MEMS has attracted worldwide interest. Figure 1 shows a typical process of a MEMS device from design goal to system integration. We can see that the structure and fabrication process of MEMS device are designed according to the design goal. Then before fabrication, we need to perform modeling to the structure. By modeling, we can estimate the performance to see if it satisfies the design goal and then optimize it to achieve the best performance. By performing modeling, substantial time and money can be saved, which increases the throughput and reduces the cost. As a result, modeling is critical for MEMS research.

Modeling applied in MEMS applications can mainly be divided into two categories, theoretical modeling and numerical modeling. The theoretical modeling is to apply exact equations to obtain exact solutions. It is a direct approach which is easy to interpret intuitively [10]. However, it has limitations that solutions can only be obtained for few standard cases, and it is incapable or difficult in the following situations: (1) shape, boundary conditions, and loadings are complex; (2) material properties are anisotropic; (3) structure has more than one material; (4) problems with material and geometric non-

linearity; (5) multiphysics situations when more than two physics are coupled together. The theoretical modeling is sometimes applied in MEMS applications when the structure is not complex, and it is also useful to verify the result of FEA.

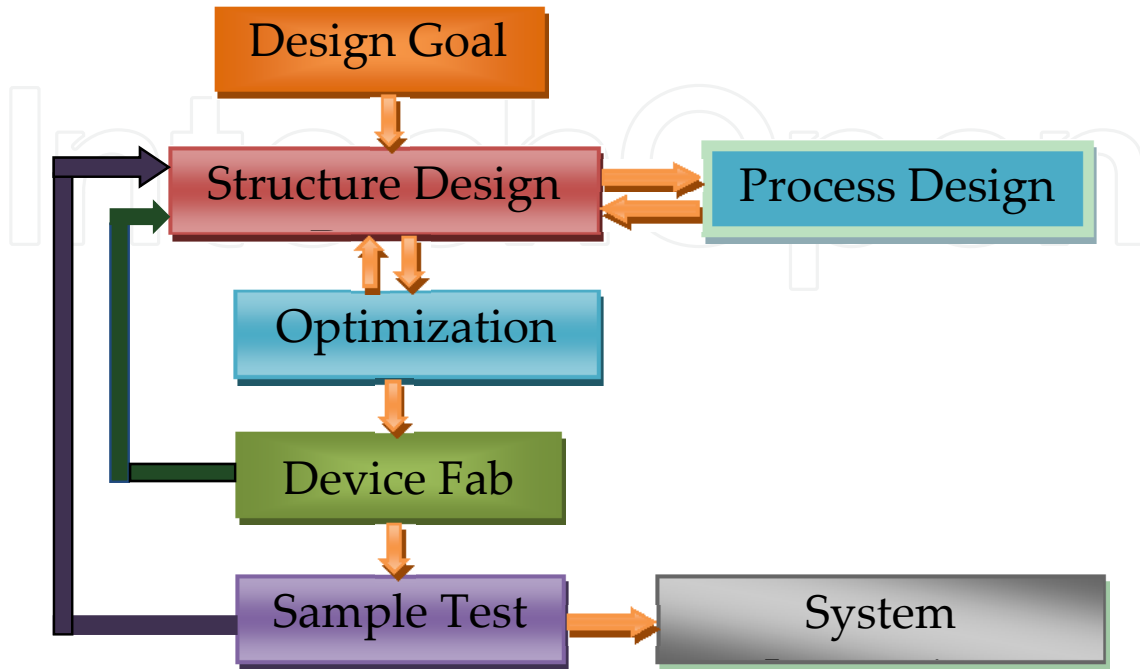


Figure 1. A schematic of a typical process of a MEMS device

Numerical modeling is to apply exact equations to obtain approximate solutions only at discrete points called nodes. Contrary to theoretical modeling, numerical modeling can handle situations which theoretical modeling is incapable. Finite Element Method (FEM) and Finite Difference Method (FDM) are two approaches most frequently used in numerical modeling. For both methods, they start from discretization, which derives the solution domain into a number of small elements and nodes. For FDM, differential equation is written for each node, and the derivatives are replaced by difference equations. In contrast, for FEM, it uses integral formulations rather than difference equations to create a system of algebraic equations, and an approximate continuous function is assumed to represent the solution for each element. The complete solution is then generated by connecting or assembling the individual solutions, allowing for continuity at the interelemental boundaries [11]. FEM have quite a few advantages over FDM [10], such as (1) it can give values at any point, while FDM can only give value at discrete node points; (2) FEM can consider the sloping boundaries exactly, while FDM makes stair type approximation to sloping; (3) FEM needs fewer nodes to get good results while FDM needs large number of nodes; (4) FEM can handle almost all complicated problems, while FDM cannot handle complicated problems, such as multiphysics simulation which is the general case in MEMS applications.

Due to the aforementioned advantages, FEA has been widely applied in MEMS applications, including electromagnetic simulation, electrothermal simulation,

thermoelectromechanical simulation, piezoelectric/piezoresistive simulation, microfluidics simulation, *etc.* Quite a few commercially available FEA softwares are readily used in MEMS applications, such as Intellisuite, ANSYS, COMSOL, Conventorware. Of them, Intellisuite is specially designated for MEMS simulation with quite a few modules, including Intellimask, Intellifab, MEMaterial, 3D Builder, Thermoelectromechanical modules, *etc.*, which has user friendly interface that users can obtain 3D structure directly from defined masks and fabrication process, and the 3D structure can be directly applied to further simulation [12]. What is more, the simulation result is quite close to experiment. In this chapter, we use Intellisuite for simulation.

In this chapter, we show the importance of FEA in MEMS research through an example of a micromachined spatial light modulator (μ SLM). Firstly we will introduce the design and operating principle of the μ SLM. Then we will introduce the modeling of the μ SLM, including theoretical modeling and FEA modeling. Following is the optimization of the μ SLM according to the modeling. Finally we present the fabrication and experiment.

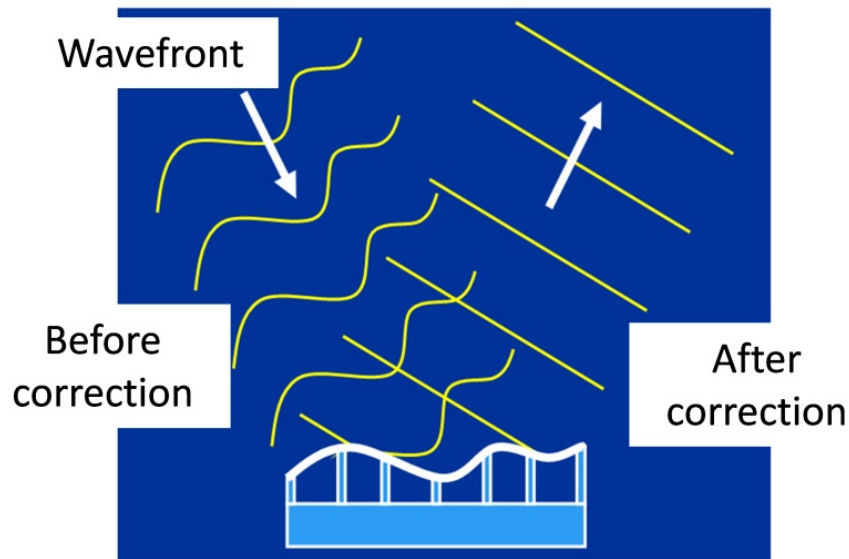


Figure 2. A schematic of the operating principle of spatial light modulator (SLM) used in Adaptive Optics systems, SLM is used to corrected the wavefront

Spatial Light modulators (SLMs) play an important role in modern technology, particularly in the field of micro-optical technology. They find applications in optical communication systems, and adaptive optics (AO) systems [13]. AO systems perform closed-loop phase correction of time-varying, aberrated wavefronts using two essential components: a wavefront sensor and a SLM [14]. A schematic of the operating principle of SLM is illustrated in figure 2. When light from stars travel through the atmosphere, aberration is induced by the turbulence in atmosphere, and the wavefront of the light is no longer a plane. If this wavefront is imaged by a telescope, a very blurry image is formed, therefore in Adaptive Optics area, researchers use SLM to correct the wavefront to be plane.

Conventional SLMs based on piezoelectric actuators cost approximately \$1000 per actuator and therefore find limited use even at major research centers [15]. In contrast, MEMS

technology offers a potentially low cost alternative to existing SLMs: the μ SLMs. A large problem for μ SLMs is their small stroke (maximum displacement), which greatly undermines the performance of the whole AO system. As a result, researchers have tried quite a few approaches to enlarge the stroke, but these approaches are difficult to implement because of either fabrication difficulty or structural complexity. As a result, we come up with a μ SLM based on the leverage principle in this chapter to solve the problem.

2. Design and modeling of the μ SLM

2.1. Design and operating principle of the μ SLM

A schematic of the μ SLM is shown in figure 3(a). It can be seen that the μ SLM is composed of four single out-of-plane actuators and one mirror plate (here only 1/4 mirror plate is shown), which are connected together by a via. From figure 2(b) we can see that one single out-of-plane actuator is composed of two anchors, two microbeams, one lower electrode, one upper electrode (serving as the short arm), and one long arm. The lower electrodes and two anchors are fixed to substrate and the long arm is connected to the two anchors by two microbeams. The size of each actuator is shown in figure 3(b). W_1 , L_1 , a , and L represent the width and the length of the upper and lower electrodes, and l_1 , b_1 , l_2 and b_2 denote the length and the width of the microbeams and long arms, respectively, while h is the thickness of the structural layer and d is the horizontal distance from the fulcrum to the central line of bottom electrode.

When the lower and upper electrodes are subjected to different potentials, electrostatic attractive force arises. A torque around the microbeams emerges and makes the upper electrode and the long arm rotate around the microbeams, as shown in figure 3(c). As a result, the end of the long arm goes upward, thus forming a lever mechanism, with the microbeams as a fulcrum. If the length of the long arm is much larger than that of the short arm, the downward displacement will be magnified to be a much larger upward displacement. At the same time, microbeams will bend down due to the moment from the electrostatic force. The total displacement of the mirror plate is the vector sum of the upward displacement caused by the rotation and the downward displacement of the microbeams (Here we assume the displacement of the mirror plate is the same as the displacement at the end of the long arm, because in MEMS applications the mass of the mirror plate can be neglected). By a proper design of the structure, the downward displacement of the microbeams will be much smaller than the upward displacement at the end of the long arm, resulting in a larger upward displacement of the mirror plate [16].

2.2. Modeling of the μ SLM

After presenting the structure and operating principle, we modeled the μ SLM both by theoretical modeling and FEA. First we carried out theoretical models. Two approaches were used in the theoretical modeling: the energy method and the superposition method.

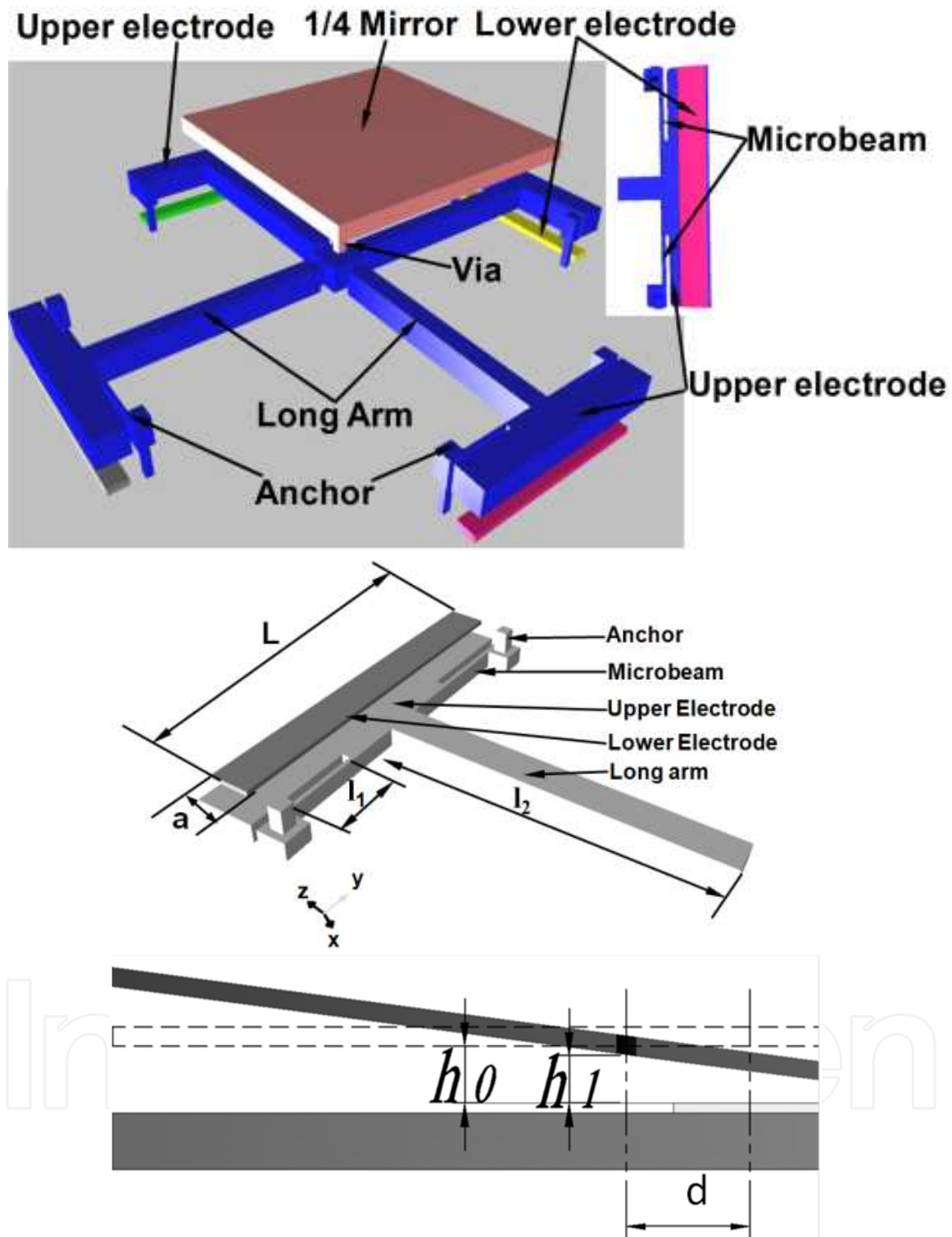


Figure 3. (a) A lateral view of a μ SLM, it is composed of four single out-of-plane actuators and one mirror plate, each single out-of-plane actuator is composed of two anchors, two microbeams, one lower electrode, one upper electrode (serving as the short arm), and one long arm, (b) A lateral view of a single out-of-plane actuator, (c) cross-section view of the single out-of-plane actuator in figure 2(b) when a voltage is applied between the lower and upper electrode, a small displacement at the end of short arm will be amplified to be a larger displacement at the end of the long arm

In the energy method, the force and moments applied to the structure is shown in figure 4. When different potentials are subjected to the upper and lower electrodes, electrostatic force arises. As mentioned above, the upper electrodes and long arms rotate around microbeams, and at the same time microbeams bend down. The force, moment and torque of anchors tend to resist this movement and the structure will ultimately reach a balance.

When a voltage V is applied to the four upper and the four lower electrodes, the electrostatic attractive force can be calculated by [16]:

$$F_e = \frac{\epsilon\epsilon_0LaV^2}{2h_0^2} \left[1 + \frac{2d}{h_0}\theta \right] \tag{1}$$

In our design, $2d/h_0=20$, and $\theta \ll 1$. In order to simplify our calculation, the second term can be omitted without bringing much error.

The electrostatic force can be simplified and rewritten as follows

$$F_e = \frac{\epsilon\epsilon_0LaV^2}{2h^2} \tag{2}$$

In order to derive the displacement at the mirror, we used Castigliano’s second theorem and set a fictitious load at the central mass, as shown in Figure 4.

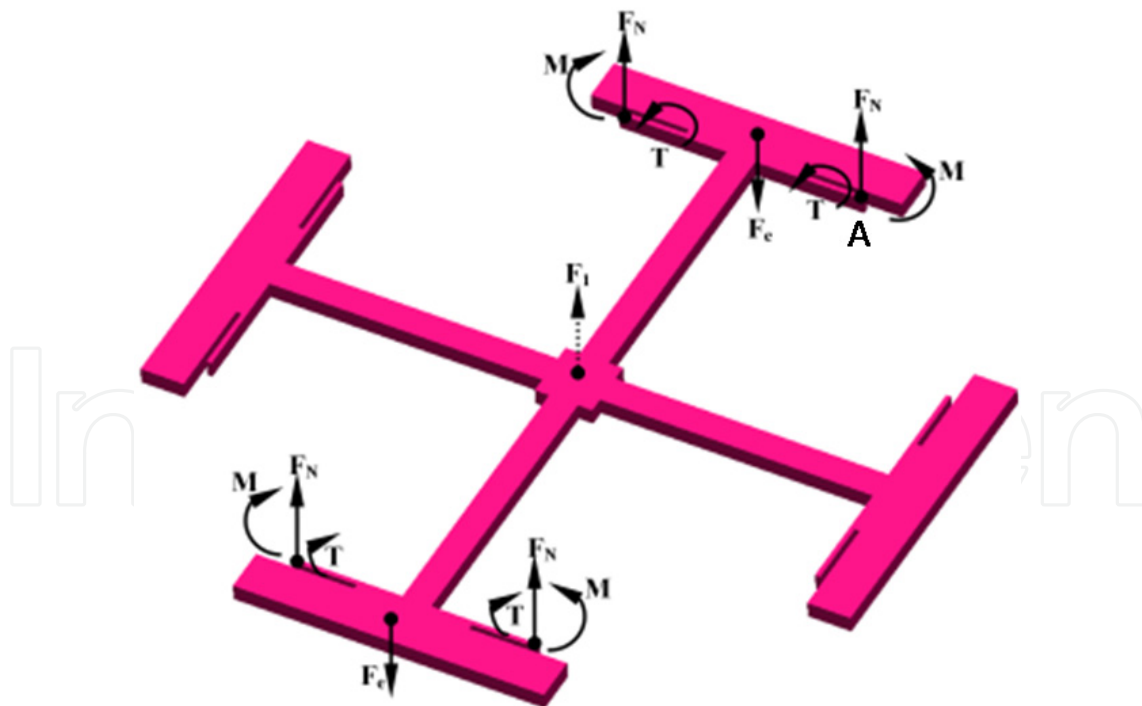


Figure 4. Mechanical model of the energy method for the μ SLM, forces, moments and torques of one single out-of-plane actuator is shown for simplification.

Considering the symmetry of the structure, the μ SLM can be divided into four single out-of-plane actuators and each one can be further subdivided into four parts: two microbeams,

one long arm and one upper electrode (short arm). In our case, the width of upper electrodes is much larger than the other three parts and the length is smaller, therefore we assume upper electrodes are rigid.

According to equations of force equilibrium, we get

$$F_N = F_e/2 - F_1/8 \quad (3)$$

As shown in figure 4, the bending moment and the torque applied to two microbeams and the long arm can be given by

$$M_1 = M_2 = F_N x - M, \quad T_1 = T_2 = T \quad (4)$$

$$M_3 = F_e(a+x) - 2F_N x - 2T = F_e a + F_1 x/4 - 2T, \quad T_3 = 0 \quad (5)$$

According to the virtual work principle, the total strain energy in one single actuator is

$$U_1 = \int_0^{l_1} \frac{M_1^2(x)}{2EI_2} dx + \int_0^{l_1} \frac{M_2^2(x)}{2EI_2} dx + \int_0^{l_2} \frac{M_3^2(x)}{2EI_1} dx + \int_0^{l_1} \frac{T_1^2(x)}{2GJ} dx + \int_0^{l_1} \frac{T_2^2(x)}{2GJ} dx \quad (6)$$

Where E , G , J , I_1 , and I_2 represent the Young's modulus, the shear modulus, the polar moment of microbeams, the inertial moment for the long arm and the microbeams, respectively.

As the total strain energy stored in the lever actuator is four times of that in single actuator, and the bending and torsional angles at point A (see in figure 4) are both zero, according to Castigliano's second theorem

$$\frac{\partial U_{total}}{\partial M} = 0, \quad \frac{\partial U_{total}}{\partial T} = 0 \Rightarrow M = \frac{1}{2} F_N l_2, \quad T = \frac{1}{8} \frac{(F_1 l_2^2 + 8F_e l_2 d) GJ}{EI_1 l_2 + 2GJ l_2} \quad (7)$$

Based on the unit-load method, equation (7) can be rewritten as

$$z = \int_0^{l_1} \frac{M_1(x)}{EI} \frac{\partial M_1(x)}{\partial F_1} dx + \int_0^{l_1} \frac{M_2(x)}{EI} \frac{\partial M_2(x)}{\partial F_1} dx + \int_0^{l_2} \frac{M_3(x)}{EI} \frac{\partial M_3(x)}{\partial F_1} dx + \int_0^{l_1} \frac{T_1(x)}{GJ} \frac{\partial T_1(x)}{\partial F_1} dx + \int_0^{l_1} \frac{T_2(x)}{GJ} \frac{\partial T_2(x)}{\partial F_1} dx \quad (8)$$

By combining the above equations to (8) and letting the fictitious load F_1 be zero, we have

$$z = -\frac{F_e l^3}{24EI_2} + \frac{1}{GJ} \frac{F_e l_1^3 l a G^2 J^2}{(EI_1 l + 2GJ l_1)^2} + \frac{1}{EI_1} \left(F_e a - \frac{2F_e l_1 a GJ}{EI_1 l + 2GJ l_1} \right) \left(\frac{l_1^2}{2} - \frac{l_1^3 GJ}{EI_1 l + 2GJ l_1} \right) \quad (9)$$

In the superposition method, the displacement of the mirror plate is the sum of the upward displacement of the mirror plate and the downward displacement of the microbeams.

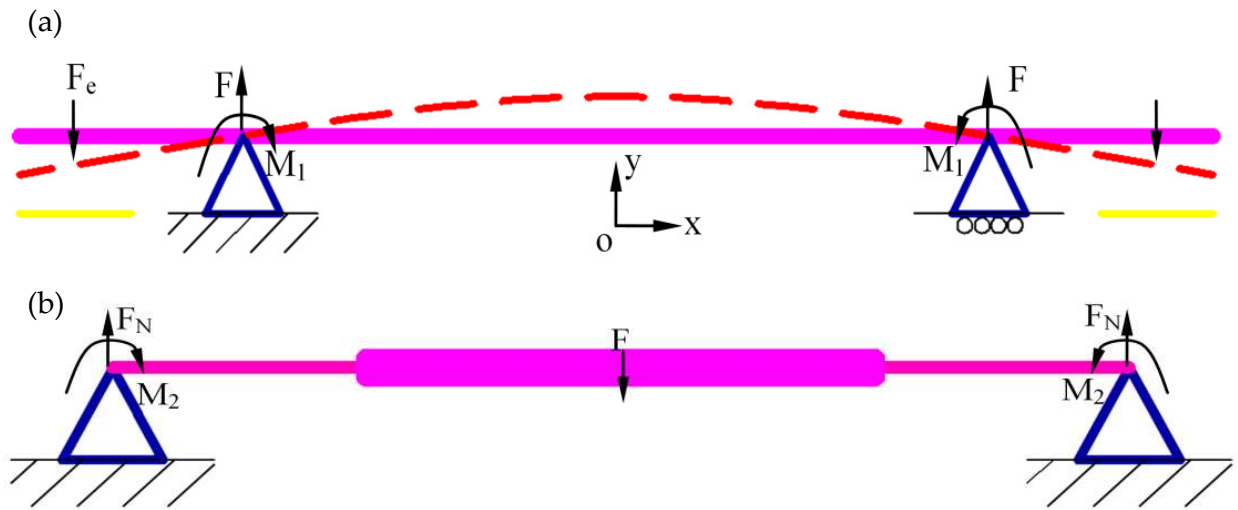


Figure 5. Mechanical model of the superposition method: (a) shows the forces and moments of the long and short arm, (b) shows the forces and moments of the 2 microbeams.

First we will analyze the force and moment applied on the long arm, as shown in figure 5. According to the boundary condition

$$y_1(0) = 0, y_1'(0) = 0, y_1'(l_2) = \theta_1, \theta_1 = M_1 l_1 / 2GI_p \tag{10}$$

We can obtain the displacement of the center of the two long arms:

$$y = \frac{1}{2} \frac{\varepsilon \omega (b-a)(b+a) V^2 l_2^2}{4h^2 EI} \left(1 - \frac{1}{1 + EIl_1 / 2l_2 GI_p} \right) \tag{11}$$

The mechanical model of 2 microbeams is illustrated in Figure 5(b). It is an indeterminate beam with variable sections, therefore we can derive the displacement of center of the two microbeams using transfer matrix method [17]. First we divide it into 4 sections. The transfer matrix from the left end of section 1 to the right end of section 4 can be obtained

$$C = A_1 \times A_2 \times B \times A_2 \times A_1 \tag{12}$$

Where A_1 , A_2 , and B are transfer matrix between left end and right of section 1, left end and right of section 2, right end of section 2 and left end of section 3, which can all be calculated by law of transfer with cross section state vector.

After applying boundary condition, $y_{1L}=0, \theta_{1L}=0, y_{4R}=0, \theta_{4R}=0$ we can calculate force and moment applied on the left end of section 1 and right end of section 4. Then substituting the force and moment to

$$C_1 = A_2 \times A_1 \tag{13}$$

We can calculate the transfer matrix from the left end of section 1 to the right end of section 2. Therefore according to

$$Z_{2R} = C_1 \times Z_{1L} \tag{14}$$

Where Z_{2R} , Z_{1L} are the section vectors of the left end of section 1 and the right end of section 2, respectively. We can calculate the displacement of the center of various section beams. By substituting parameters in to these equations, we calculated that the downward displacement is 32.4 nm when applied a voltage of 20 V.

Finally the displacement calculated by the superposition method is derived as

$$z = \frac{1}{2} \frac{\varepsilon w a W_1 V^2 l_1^2}{2 h^2 E I_1} \left(1 - \frac{1}{1 + E I_1 l / 2 l_1 G J} \right) - y_2 \tag{15}$$

Here y_2 is calculated by the transfer matrix method.

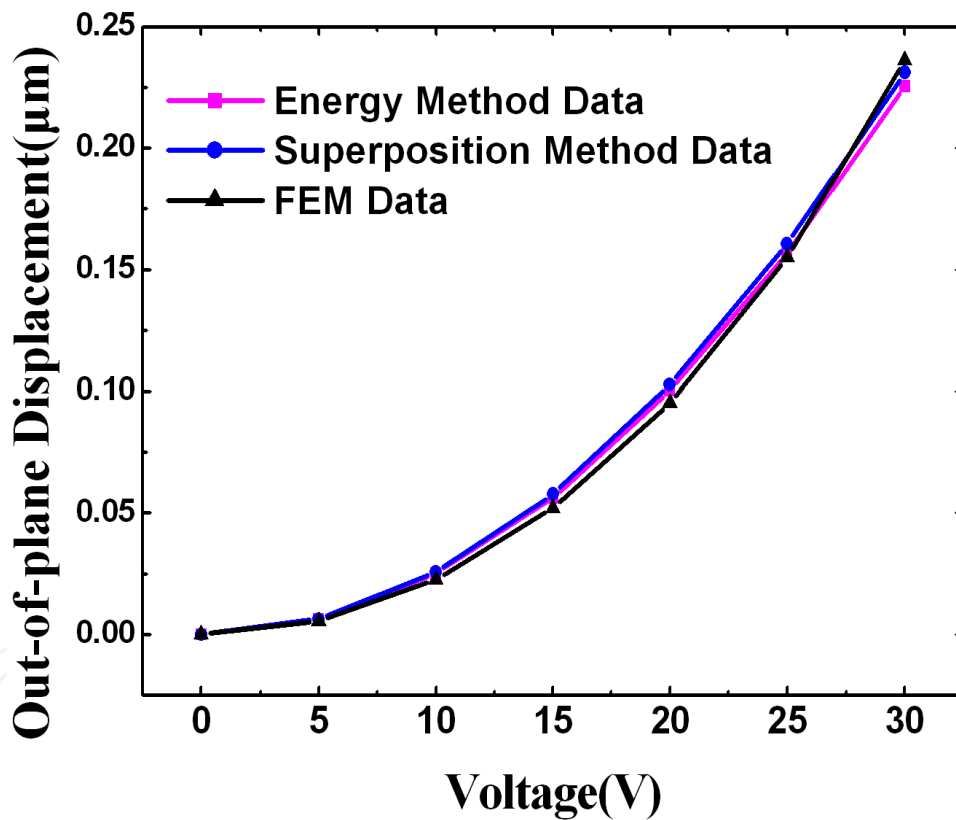


Figure 6. Results of the two theoretical models and FEA results, the discrepancy between theoretical modeling and FEA is small

After deriving the theoretical models, we carried FEA modeling using Intellisuite. Then the FEA result is validated the theoretical modeling by comparing them with FEA. As shown in figure 5, both the two theoretical models are in good agreement with FEA, and this validates the results of the theoretical modeling and FEA. Then we combined the theoretical modeling and FEA to optimize the structure.

3. Structure optimization

In this section, we discuss the optimization of the structure, including the optimization of the microbeams, the long arm, the end of the long arm, the connection between the four single out-of-plane actuators, and the upper electrode.

3.1. The long arm

3.1.1. Width of the long arm

When studying the influence of the width of the long arm, we calculated the differential of equation (9) to b_2

$$\frac{\partial z}{\partial b_2} = \frac{\partial z}{\partial I_1} \frac{\partial I_1}{\partial b_2} = -\frac{1}{2} \frac{EF_e l_1^2 l_2^2 a}{(EI_1 l_1 + 2GJl_2)^2} \frac{h^3}{12} \tag{16}$$

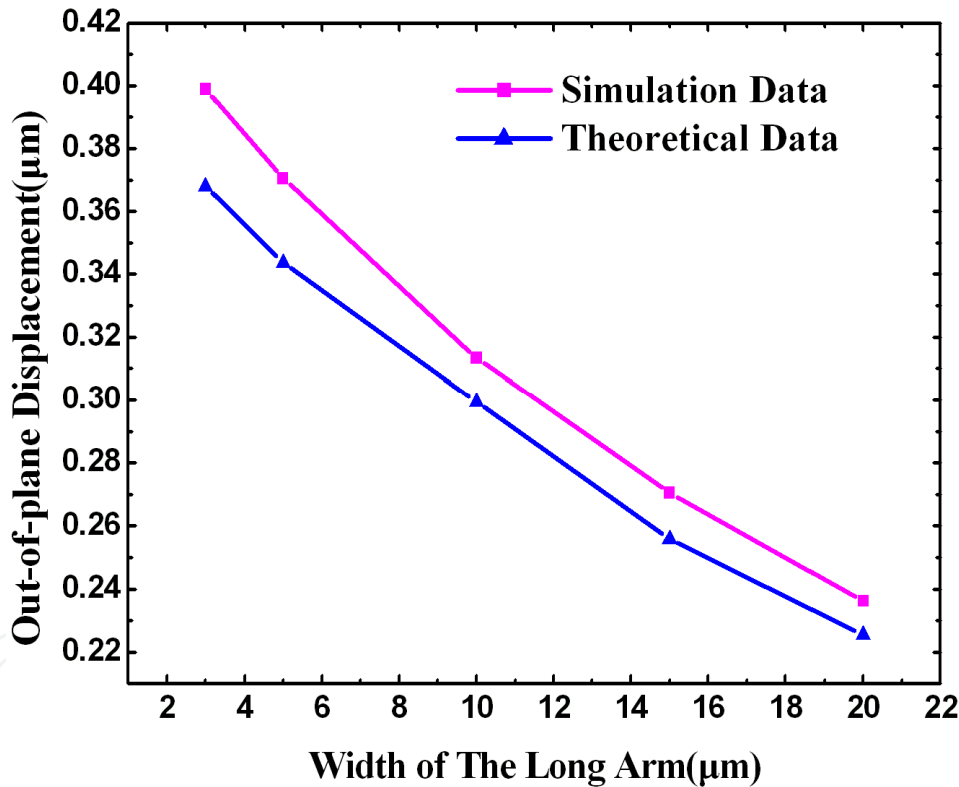


Figure 7. Theoretical and simulation data of width of long arm versus displacement, as the with of the long arm increases, the displacement decreases

It is obvious that the differential is constantly negative. Therefore the larger the width of the long arm, the smaller the displacement is when subjected to the same voltage. The simulation and theoretical data of the mirror plate displacement versus the width of long arm is shown in figure 7. Therefore as the long arm becomes wider, the out-of-plane displacement decreases. However, if the width of the long arm is very small, it tends to be more fragile and more likely to break during fabrication and test.

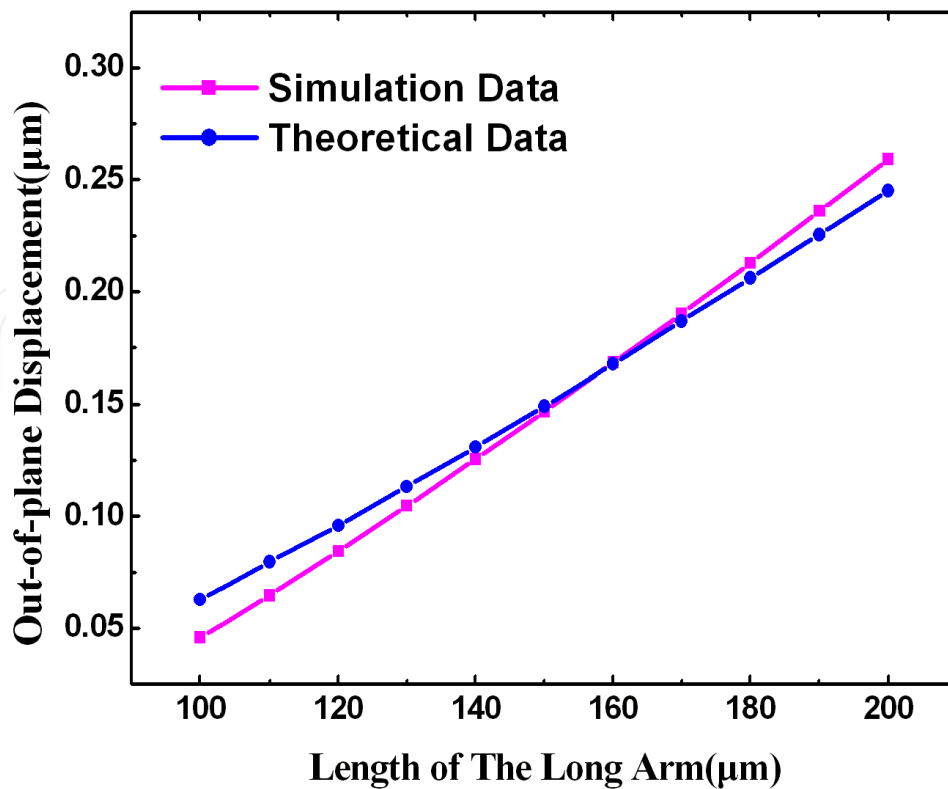


Figure 8. Theoretical and simulation data of length of long arm versus displacement, as the length of the long arm increases, the out-of-plane displacement increases

3.1.2. Length of the long arm

Then the influence of the length of the long arm is discussed. As it is well known, the longer the long arm is, the larger out-of-plane displacement will be. The simulation and theoretical displacement are in good agreement with what is expected, as shown in figure 8. However, as mentioned above, a too long arm is very fragile and is more likely to be broken.

3.2 .The microbeams

After deriving characteristics of long arm, we went on with the microbeams. In this section, the influence of the width and length of microbeams is discussed. First, we come to the width of microbeams. It's easy to see that as the width of microbeam becomes larger, so does the torsional stiffness, which will thwart the rotation of the microbeams and make the out-of-plane displacement smaller. This is verified by FEA.

Second, the influence of the length of microbeams is discussed. Figure 9 is the simulation data of out-of-plane displacement versus microbeam length. As the microbeam length increases, so does the out-of-plane displacement, however, the increase rate slows down. This is because when the length of microbeam is small, the torsional stiffness is relatively larger, as mentioned above, thwarting the microbeams from rotating. In contrast, as the length increases, the downward bending displacement of microbeam increases, as shown in

equation (9). As a result, the upward displacement is partly offset by downward bending of microbeams.

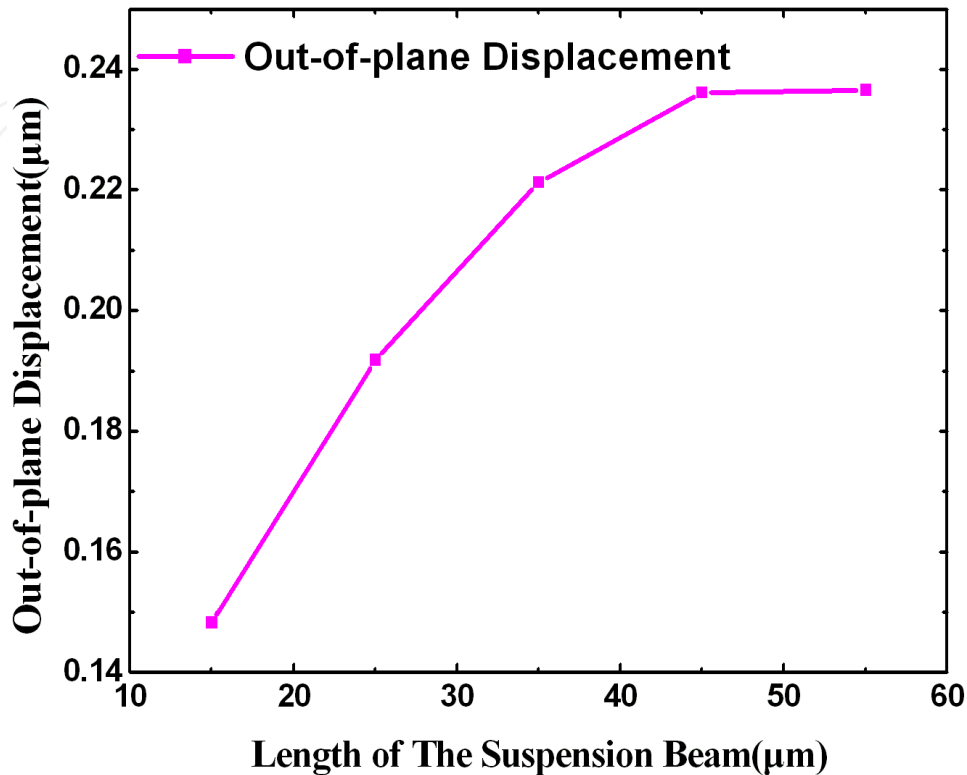


Figure 9. Simulation data of length of microbeams versus displacement, displacement increases with the increase of the length of microbeams, and the rate of increment slows down gradually.

There is one thing to notice when the microbeams are too short. When applied a relatively high voltage, the microbeams may fracture due to torsional stress. According to mechanics of materials, the maximum torsional stress can be calculated as follows

$$\tau_{\max} = \frac{T}{\alpha b_1 h^2} \quad (17)$$

where τ_{\max} , α , T , b_1 and h represent the maximum torsional stress, coefficient related to b_1/h , torque of the microbeams, width and height of microbeams. Also we know that

$$\theta = \frac{Tl_1}{GJ} \quad (18)$$

where θ and T are rotational angle and torque, respectively.

Assuming the end of short beam has a displacement of $0.5 \mu\text{m}$, the rotation angle is about 0.0125 radian, then it can be calculated that $\tau_{\max}=45.97$ MPa. Here the parameters we use are

$\alpha=0.231$, $G=65$ GPa. According to ref. [18], using these two equations above, we calculate that $\tau_{\max}=60.2$ MPa and the portion of stress-strain curve is about 0.00076. We set $G=79$ GPa [19] and $\alpha=0.299$, other parameters are based on reference [19]. Then according to reference [19], the fracture stress of polysilicon is two to ten times smaller than single crystal silicon, therefore at this time, when microbeam is shorter than $22.9 \mu\text{m}$, it will fracture when applied a high voltage.

3.3. The end of the long arm

According to theoretical modeling and FEA, we found that the end of the long arm greatly confines the displacement. As a result, we made three optimizations to the structure.

First, we presented a long arm with variable sections. The structure of the long arm is shown in figure 10, which consists of two different sections, one has a width of $3 \mu\text{m}$ and the other $20 \mu\text{m}$. The total length of the two sections is set to be $190 \mu\text{m}$. When the length of the thin $3 \mu\text{m}$ width section changes, the theoretical calculation and simulation of the thin long arm length versus the displacement is plotted in figure 11, the theoretical data is calculated using equation (A. 4) (appendix) in reference [16]. We can see that the displacement of the mirror plate increases remarkably when the length of thin long arm varies from $0 \mu\text{m}$ to $40 \mu\text{m}$, this is attributed to the fact that the implementation of a thin long arm at the end of long arm makes the confinement of opposite levers to decrease, therefore, it makes the long arm easier to rotate. In contrast, the displacement changes little, just from $0.5 \mu\text{m}$ to $0.54 \mu\text{m}$, when the length of thin long arm varies from $40 \mu\text{m}$ to $120 \mu\text{m}$. This is because when the length of thin long arm increases, the confinement of the end of long arms decreases, it makes the out-of-plane displacement to increase. However, when the thin long arm become longer, the bending of the long arm increases and this makes the out-of-plane displacement decrease. The increased displacement, which is caused by a decreased confinement, is pulled back by the decrease displacement caused by the increased bending for longer thin arms. When the thin long arm is longer than $120 \mu\text{m}$, the out-of-plane displacement demonstrates a remarkable decrease, as this thin long arm makes too much bending. Since it doesn't change much from $40 \mu\text{m}$ to $120 \mu\text{m}$, we set the thin long arm $44 \mu\text{m}$, for the reason that according to design rules, the shorter the thin long arm, the more robust it is in fabrication. This is the first structure after optimization (Structure 1).

The second optimization of the structure was to add a crab-leg beam, as illustrated in figure 12. By this means, the structure is more compact while at the same time achieving a larger displacement. We can see that both the displacement and amplification factor increase as the length of the crab-leg beam becomes longer. As a result, we set the length of the crab-leg beam to be $66 \mu\text{m}$ according to design rules, and we obtained the second optimized structure (Structure 2). The third optimization was to add a gimbal-like serpentine beam, as demonstrated in figure 13 [11]. This further reduces the confinement of the end of the long arm, thus achieving a larger displacement.

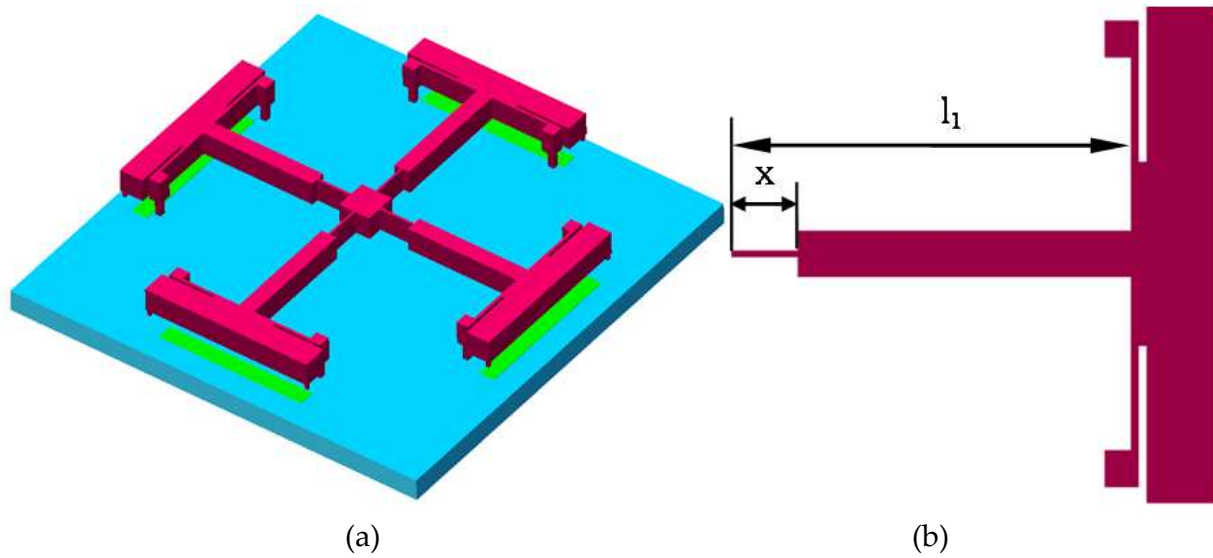


Figure 10. Schematic of the first optimized structure: (a) Lateral view of the structure in optimization, (b) Top view of a single actuator in optimization

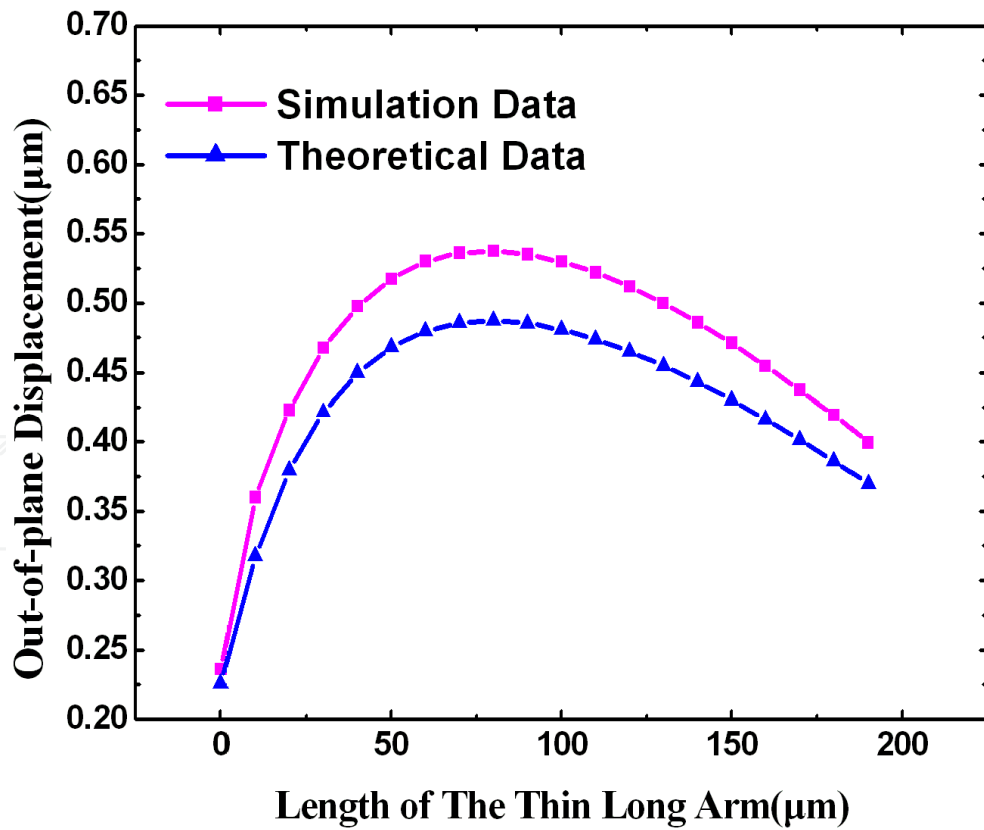


Figure 11. Theoretical and simulation data of length of thin long arm versus displacement, as the length of the thin long arm increases, the displacement firstly increase, then after hitting a maximum, it decreases as length of thin long arm increase

3.4. The connection between the four single out-of-plane actuators

After optimizing the end of the long arm, we investigated the connection of four actuators. It is found that the first mode of the natural frequency of the structure 3 was the rotation along the dotted line l_1 and l_2 in figure 13, other than the out-of-plane movement. This was because there was only one connection in the structure, and the restriction to this mode was smaller than the mode of out-of-plane movement. This was not desirable for inducing mechanical instability when working at a high frequency. We made an optimization to the structure, by making four separate connections to connect the four actuators to the mirror, as depicted in figure 13. Through this method, we can enlarge the restriction of the first mode, thus making out-of-plane mode to be the first mode. After this optimization, the piston mode became the first mode, which had a resonant frequency of 4.8 kHz.

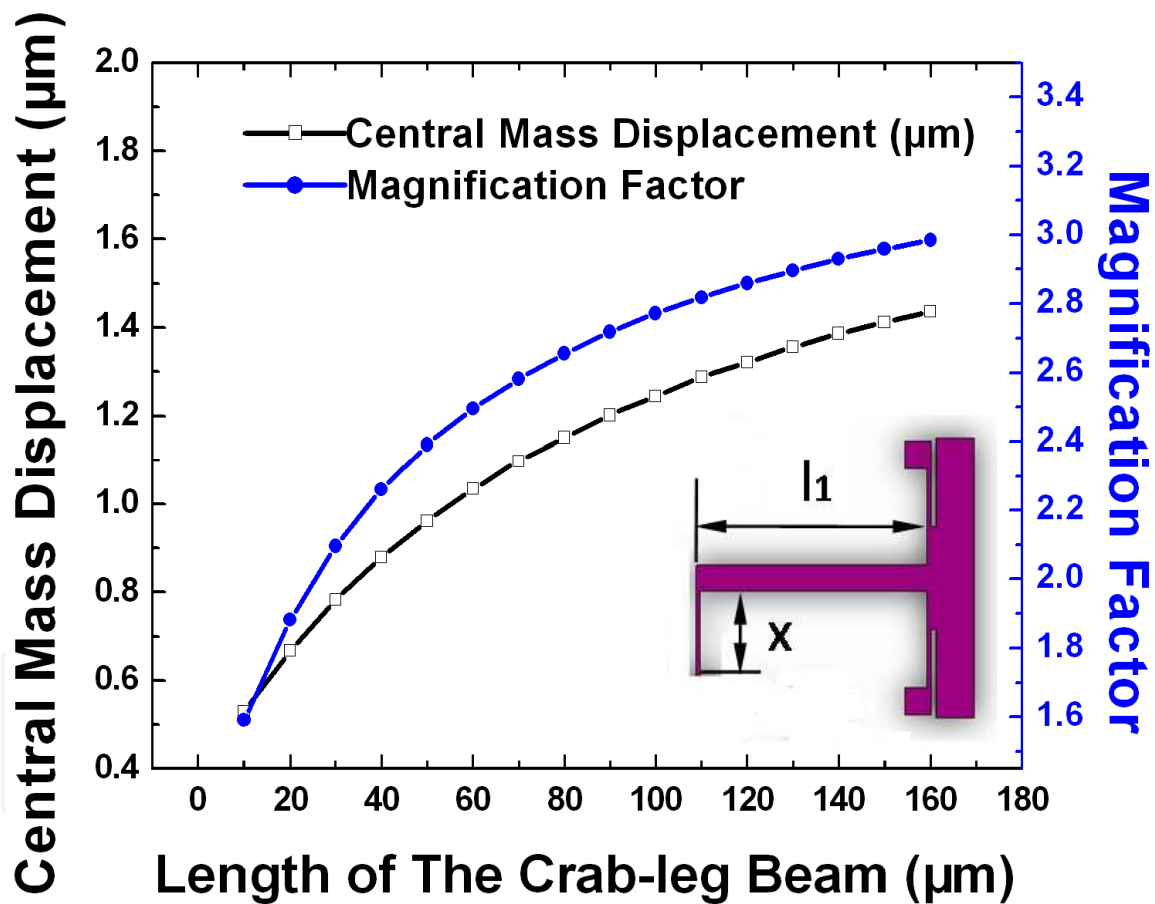


Figure 12. Displacement and Magnification factor of the second optimized structure

3.5. The upper electrode

Then we made an optimization to the upper electrode by introducing the third layer polysilicon to the upper electrode, thus enlarging the gap from 2 μm to 2.75 μm, as illustrated in figure 13, by this approach, we obtained the third optimized structure (Structure 3).

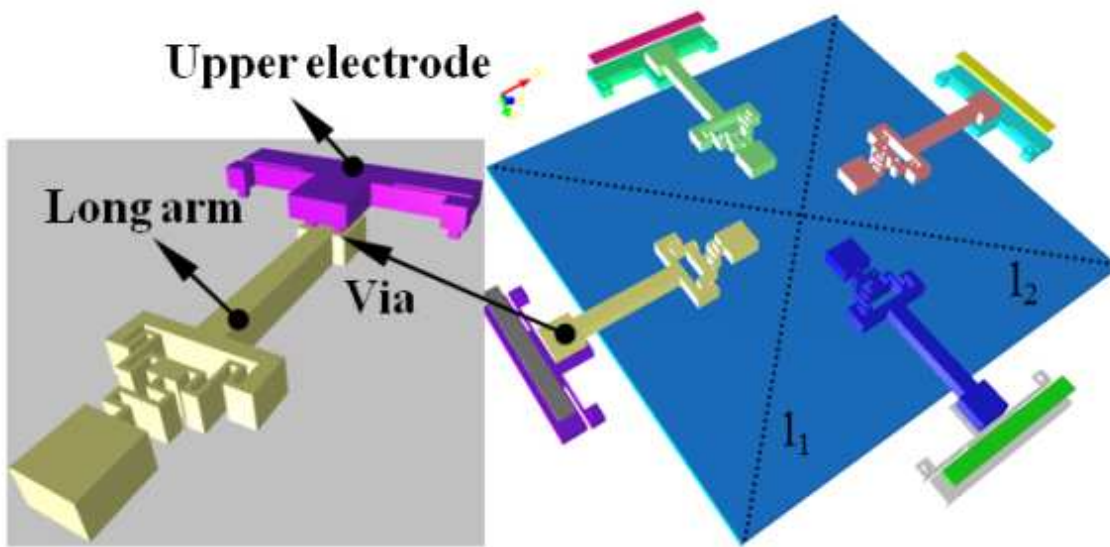


Figure 13. Lateral view of the third optimized μ SLM

3.6. Results after optimization

The results after optimization is shown in figure 14. From this figure we can see that after optimization, the maximum displacement are $1.58 \mu\text{m}$, $1.87 \mu\text{m}$, and $4.5 \mu\text{m}$, which are 3.04, 3.6, 8.65 times, respectively, higher than the structure before optimization. After optimization, we did experiment on the fabrication and test of the structures.

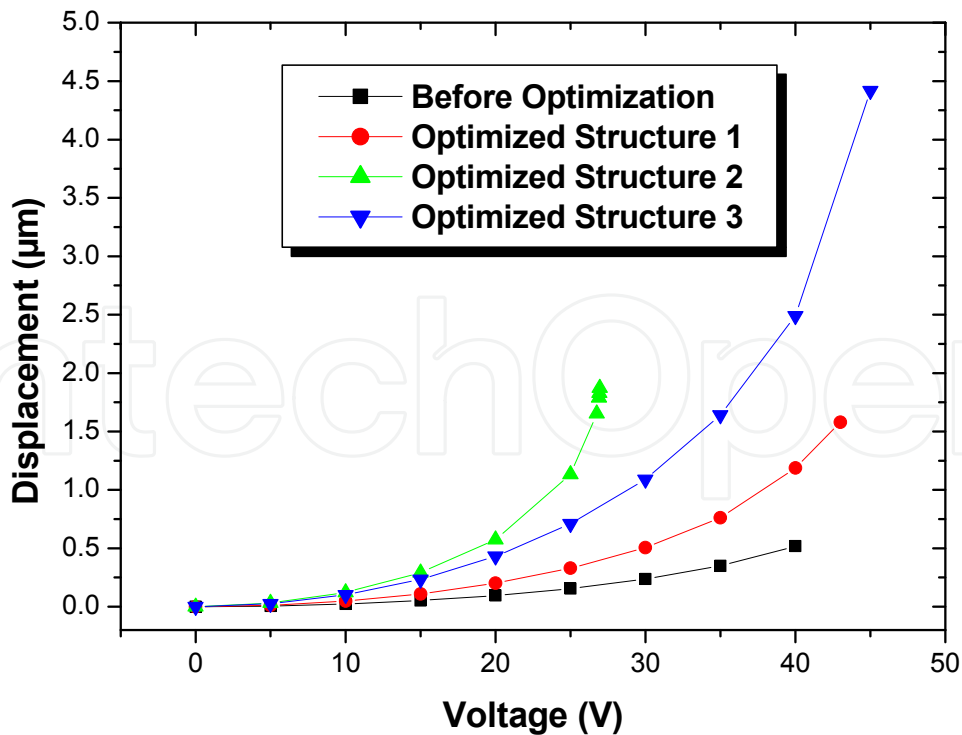


Figure 14. Simulation results before and after optimization, after optimization, the maximum displacement are $1.58 \mu\text{m}$, $1.87 \mu\text{m}$, and $4.5 \mu\text{m}$, which are 3.04, 3.6, 8.65 times higher than the structure before optimization

4. Fabrication and test

The three optimized structures were fabricated by a three-layer polysilicon surface microfabrication process. First of all, 600 nm low-stress silicon nitride is deposited on an n-type (100) wafer with a diameter of 150 mm to form electrical isolation layer. Then 500nm polysilicon film is deposited as the first polysilicon layer (Poly0). Afterward, Poly0 is patterned by photolithography and etched. Then 2 μm of phosphosilicate glass (PSG) is deposited as sacrificial layer. Then the first silicon dioxide layer (Oxide1) is patterned by lithography and etched to form dimples. The following step is to deposit a 2 μm polysilicon layer (Poly1) as the second polysilicon layer, which is etched afterwards to form the leverage mechanism. At last the Oxide1 layer is sacrificed in a bath of 49% HF to release the structural layer and the structure is dried by supercritical CO_2 drying technique. Figure 16 shows the SEM photograph of the structures. We can see the shapes of the structures are good with little curvatures, indicating that the stress gradient and stress variation along the beams is negligible.

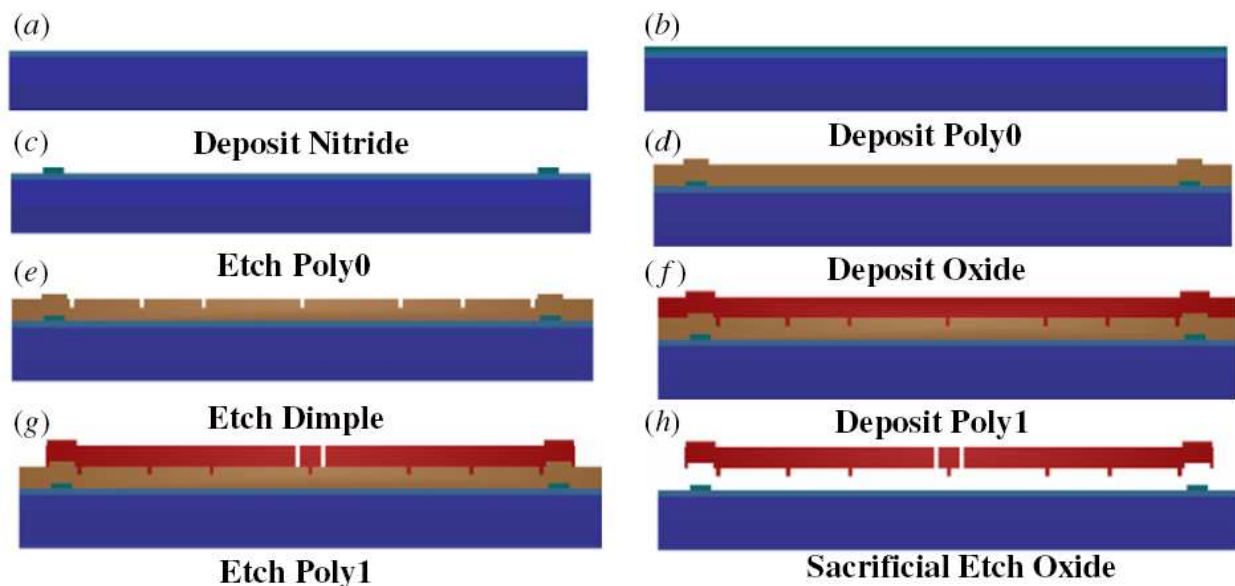


Figure 15. Fabrication process of the μ SLM, this is a three-layer surface microfabrication process, and this schematic is based on the fabrication of the first optimized structure

Then we use an optical interferometer to measure the displacement versus voltage for the three optimized structures. The test is performed using the Zygo Newview 7300 (Zygo Inc., CT, USA) A light source, in this case an incoherent broadband LED light source is split at the objective so that some of the light passes to a reference mirror and some is focused onto the surface of the sample under measurement. Light from the mirror (embedded into the interference lens) and the sample surface is reflected back into the instrument and imaged onto a camera. If the distances from the light splitter to the mirror and from the splitter to the surface are equal so that there is no optical path difference (OPD) then the camera will observe an interference pattern. This occurs when the objective is held so that the focal plane of the objective lies in the same plane as the surface. In order to perform a measurement of

the surface observed by the field of view of the objective, the objective lens is translated vertically and linearly so that the focal plane moves through the entire height range of the surface being measured. As it does so, the interference fringes will move and follow the height profile of the surface and this information is processed by the instrument to calculate the height profile to a very high precision (0.1 nm).

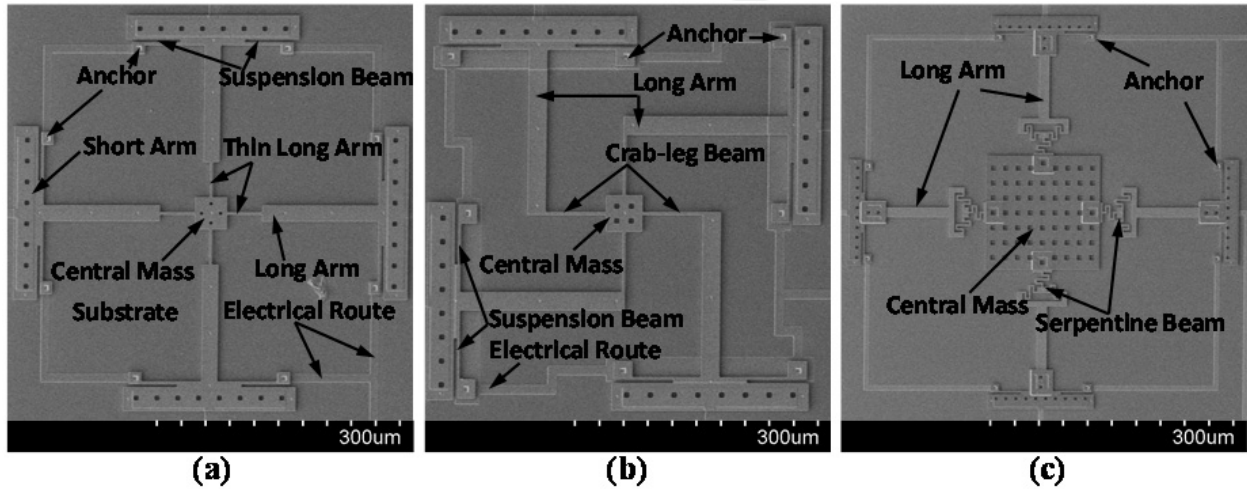


Figure 16. SEM photographs of the three optimized structures

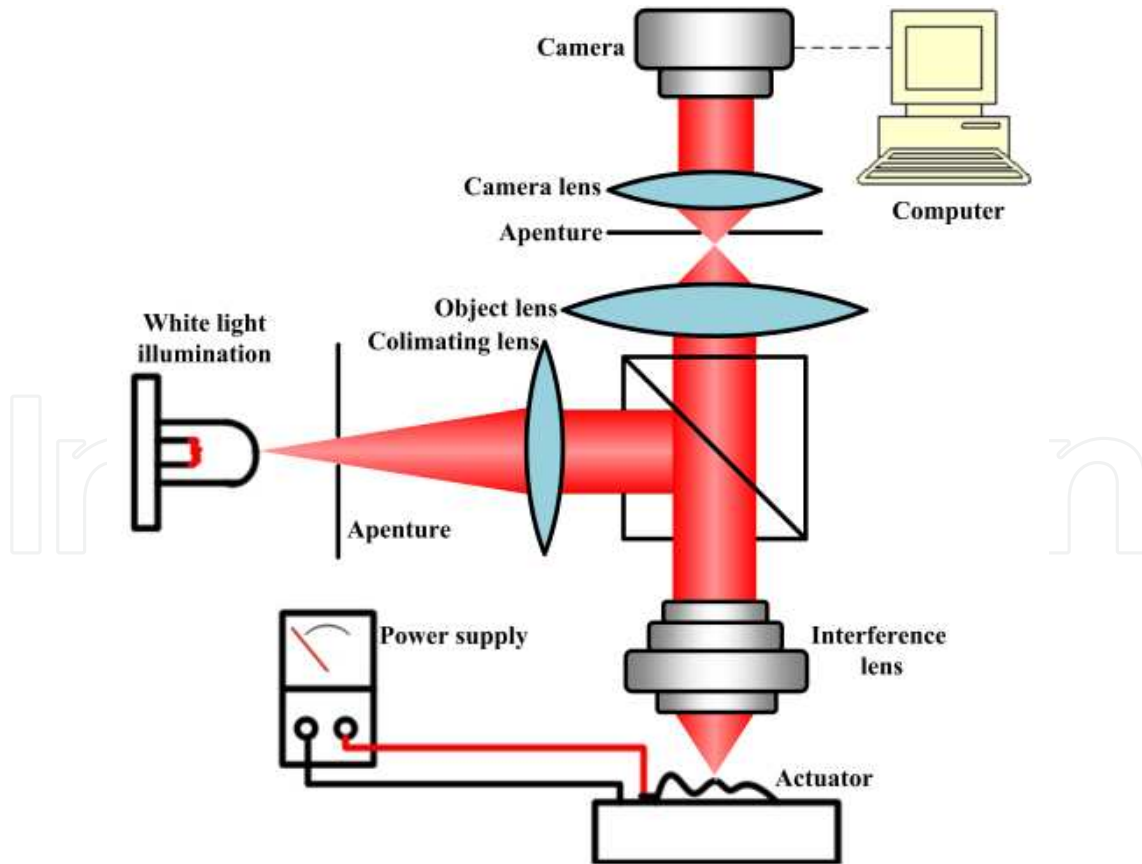


Figure 17. Optical configuration of the white light interferometer

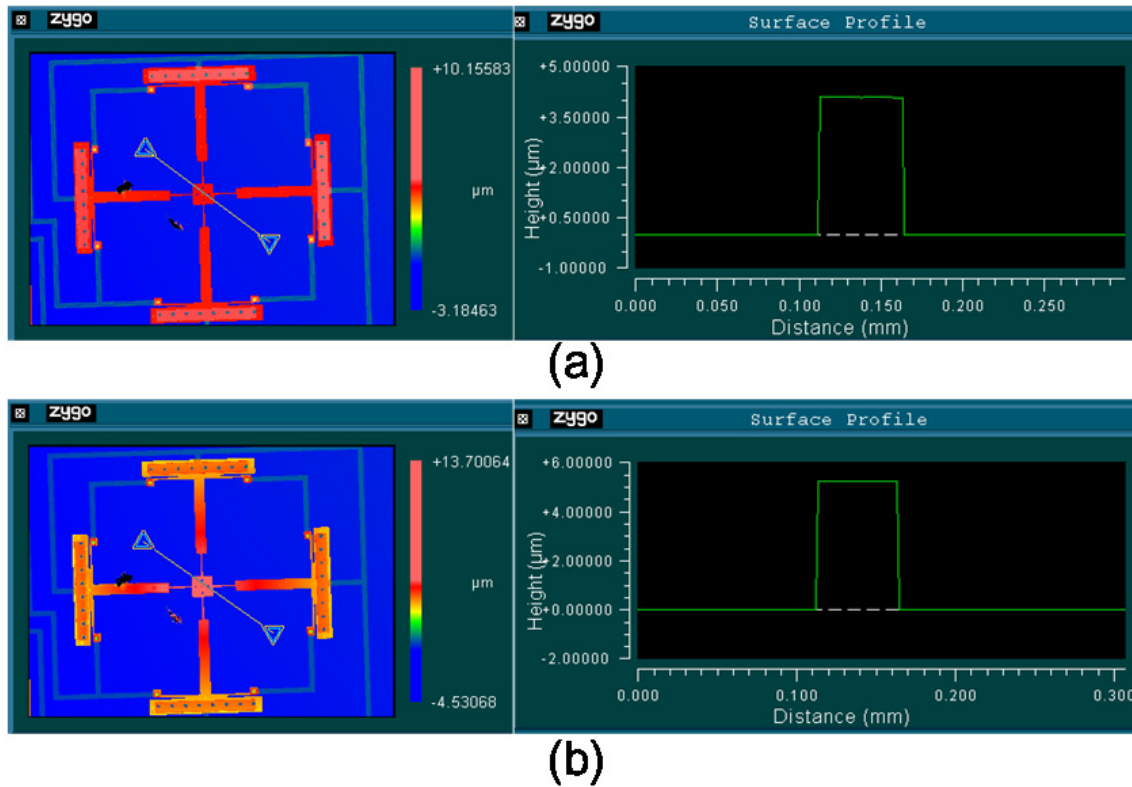


Figure 18. Optical profiles for Structure 1 before and after deformation: (a) Optical profile before applying voltage, we can see the profile is approximately a plane (b) Optical profile when applied a voltage of 47 V, we can see the short arm goes down and the long arm and central mass goes up.

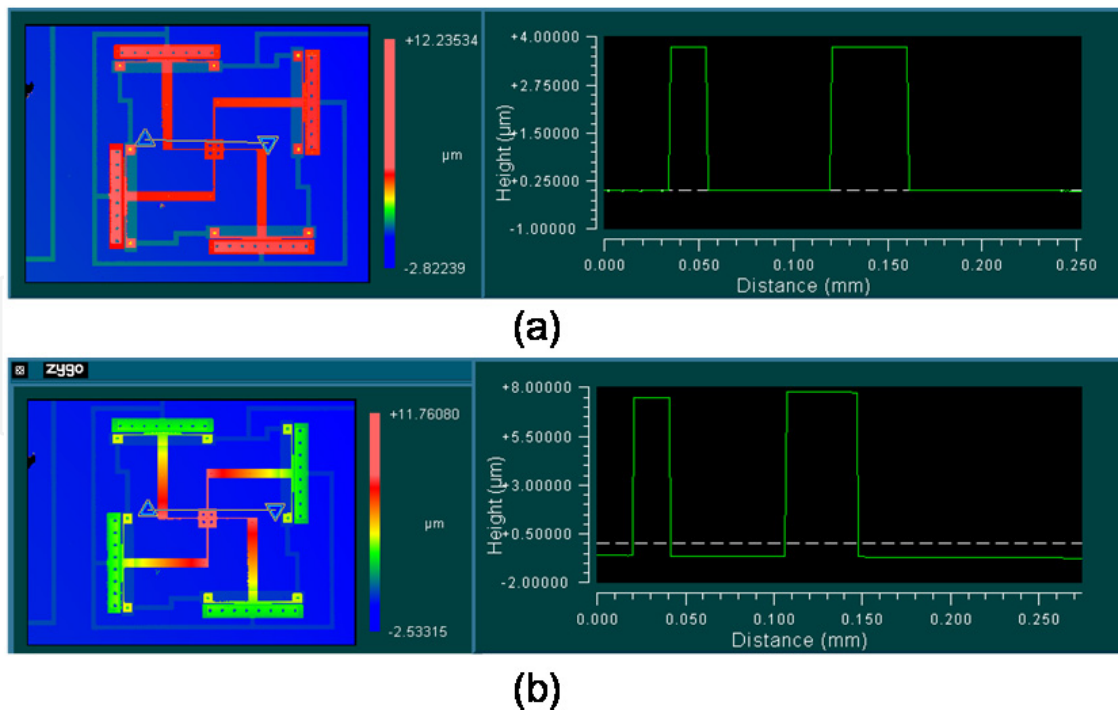


Figure 19. Optical profiles for Structure 2 before and after deformation: (a) Optical profile before applying voltage, we can see the profile is approximately a plane (b) Optical profile when applied a voltage of 24.75 V, we can see the short arm goes down and the long arm and central mass goes up.

The optical profile of Structure 1 before and after applying voltage is shown in figure 18. Before applying voltage, the structure profile is approximately a plane. Then after applying a voltage of 47 V, due to the electrostatic force, the upper electrode (short arm) goes down and the long arm and central mass goes up. Similar result is observed for Structure 2, as shown in figure 19. For the Structure 3, after applying voltage, the mirror plate did not go up, instead, it went down. After analysis, we believe there may be problem for the isolation of the mirror plate and the substrate. We will fix this problem in the future.

The displacements versus voltage for the first two optimized structures are shown in figure 20. We can see that the two optimized structures can obtain a stroke of $1.45\mu\text{m}$, and $2.21\mu\text{m}$, which are more than two times, and three times larger, respectively, than the stroke before optimization. Through this example, we can clearly see the importance of FEA in MEMS research: it saves time and money, while at the same time can handle complex/nonlinear structures.

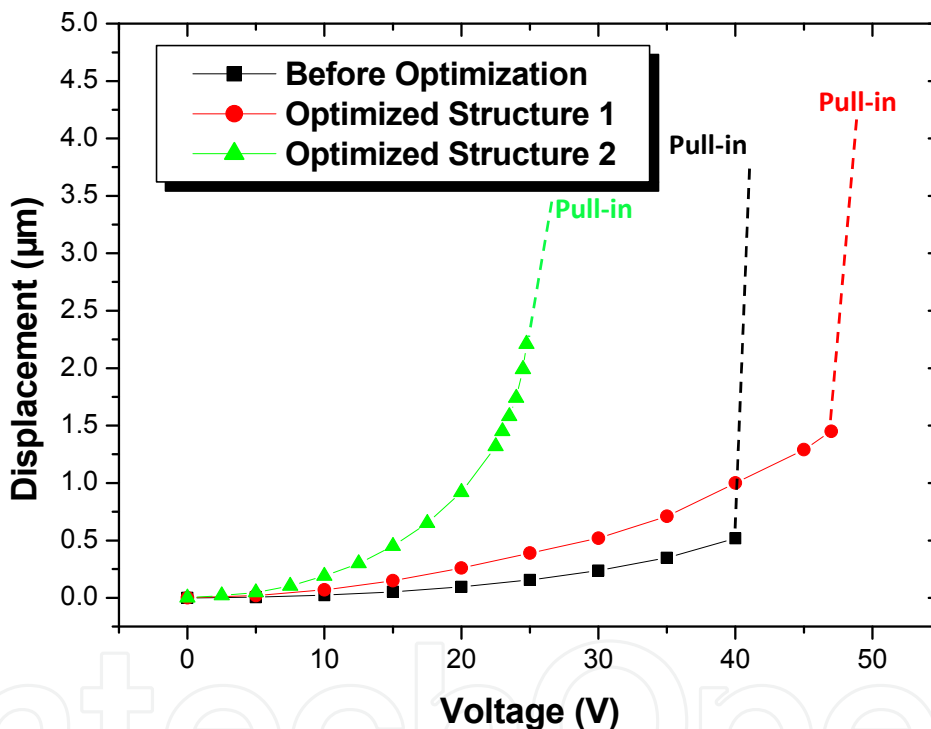


Figure 20. Experimental results of the first two structures after optimization in comparison with the structure before optimization, the maximum displacement is more than two and three times larger than the maximum displacement before optimization.

5. Conclusion

In this chapter we mainly discussed the significance of FEA in MEMS research through an example of a micromachined spatial light modulator (μSLM). We have used FEA to model the μSLM structure, verify theoretical models, and perform optimizations. After fabrication, we found that the stroke after optimization was more than 3 times larger than the stroke before optimization. As is demonstrated, FEA makes MEMS research to be time and cost efficient and thus has been widely applied in MEMS research.

Author details

Hao Ren

State Key Lab of Optical Technologies for Microfabrication, Institute of Optics and Electronics, Chinese Academy of Sciences, Chengdu, China

School of Electrical, Computer, and Energy Engineering, Arizona State University, Tempe, AZ, USA

Jun Yao

State Key Lab of Optical Technologies for Microfabrication, Institute of Optics and Electronics, Chinese Academy of Sciences, Chengdu, China

6. References

- [1] R.P. Feynman, There is plenty of room at the bottom. *J. Microelectromech. Syst.* 1 60-66 1992
- [2] D.J. Nagel and M. E. Zaghoul, MEMS: micro technology, mega impact. *IEEE Circuits Devices* 17 14-25 2001
- [3] N. Yazdi, F. Ayazi and K. Najafi Micromachined Inertial Sensors. *Proceedings of IEEE* 86(8): 1640-1659 1998,
- [4] J. Chae, H. Kulah and K. Najafi, A monolithic three-axis micro-g micromachined silicon capacitive accelerometer. *J. Microelectromech. Syst.* 14 (2): 235-242 2005
- [5] B. Piekarski, D. Devoe, M. Dubey R. Kaul and J. Conrad, Surface micromachined piezoelectric resonant beams filters, *Sensors and Actuators A: Physical*, 91:313-320 2001
- [6] J.Y. Park, G.H. Kim, K.W. Chung and J.U. Bu, Monolithically integrated micromachined RF MEMS capacitive switches, *Sensors and Actuators A: Physical*, 89:88-94 2001
- [7] M. B. Kassem and R.R. Mansour, Two movable-plate nitride-loaded MEMS variable capacitor, *IEEE Transactions on Microwave Theory and Techniques*, 52(3):831-837 2004
- [8] L.J. Hornbeck, W.E. Nelson, Bistable deformable mirror device. *OSA Technological Digest Series*, 86:1687-1704 1988
- [9] J.M. Younse, Mirrors on a chip, *IEEE Spectrum*, 30:27-31 1993
- [10] S.S. Bhavikatti. *Finite Element Analysis*. New age international publishers, New Delhi 2005
- [11] S. Moaveni. *Finite element analysis, Theory and Application with ANSYS*. Prentice Hall, Upper Saddle River, New Jersey 1999
- [12] <http://www.intellisense.com/>
- [13] H. Ren, Z.G. Ni, J.M. Chen, A.L. Gong and J. Yao, A micro spatial light modulator based on leverage principle, *Key Engineering Materials* 483:137-142 2011
- [14] R.K. Tyson, *Principles of Adaptive Optics* (2nd ed.), Academic Press, New York 1998
- [15] N. Doble, M. Helmbrecht, M. Hart and T. Juneau, Advanced wavefront correction technology for the next generation of adaptive optics equipped ophthalmic instrumentation. *Proc. SPIE* 5688 125-132 2005

- [16] H. Ren, F.G. Tao, W.M. Wang and J. Yao, An out-of-plane electrostatic actuator based on the lever principle, *J. Micromech. Microeng.* 21 045019 2011
- [17] S. Timoshenko and J. N. Goodier, *Theory of Elasticity*, McGraw-Hill, New York, 1951.
- [18] J. M. Gere and S. P. Timoshenko *Mechanics of materials* 2nd edition (Brooks/Cole Engineering Division) 1984
- [19] W. Alexander and S. Harald. Torsional stress, fatigue and fracture strength in silicon hinges of a micro scanning mirror *Proc. of SPIE* 5342:176-185 2004

IntechOpen

IntechOpen